Physica A 389 (2010) 1607–1618

Contents lists available at ScienceDirect

Physica A

journal homepage: www.elsevier.com/locate/physa

Continuum reconstruction of the pore scale microstructure for Fontainebleau sandstone

F.D.E. Latief [a,b], B. Biswal [a,c,*], U. Fauzi [b], R. Hilfer [a,d]

[a] ICP, Universität Stuttgart, Pfaffenwaldring 27, 70569 Stuttgart, Germany

[b] Physics of Complex Systems, Faculty of Mathematics and Natural Sciences, Bandung Institute of Technology, 40132 Bandung, Indonesia

[c] S.V. College, University of Delhi, New Delhi - 110 021, India

[d] Institut für Physik, Universität Mainz, 55099 Mainz, Germany

ARTICLE INFO

Article history:
Received 11 May 2009
Received in revised form 24 October 2009
Available online 22 December 2009

Keywords:
Sandstone
Image reconstruction
Tomography

ABSTRACT

A stochastic geometrical modeling technique is used to reconstruct a laboratory scale Fontainebleau sandstone with a sidelength of 1.5 cm. The model reconstruction is based on crystallite properties and diagenetic parameters determined from two-dimensional images. The three-dimensional pore scale microstructure of the sandstone is represented by a list of quartz crystallites defined geometrically and placed in the continuum. This allows generation of synthetic μ-CT images of the rock model at arbitrary resolutions. Quantitative microstructure comparison based on Minkowski functionals, two-point correlation function and local porosity theory indicates that this modeling technique can provide more realistic and accurate models of sandstones than many existing techniques used currently. Synthetic μ-CT images at different resolutions from a laboratory scale model of Fontainebleau sandstone are made available to the scientific community for resolution dependent petrophysical analysis.

1. Introduction

The pore scale microstructure of porous media correlates strongly with their macroscopic physical properties such as conductivity, permeability, formation factor, elastic moduli etc. [1,2]. Representative microscopic models have been frequently employed to make quantitative prediction of the petrophysical parameters and to simulate fluid flow in such systems [3–11]. A widely used experimental model is the digitized three-dimensional (3D) images obtained from the microcomputer tomography (μ-CT) procedure [12]. Although it provides reasonably accurate 3D representation of the pore space microstructure for sandstones, access to such an experimental procedure is both difficult and expensive. Computerized reconstructed models of porous media have tried to fill this gap as they can be created with information from two-dimensional (2D) microscopic images. These 2D images can be easily obtained at high resolutions.

The reconstruction of porous media is of great interest in diverse fields, e.g. earth science, engineering, material science, biology, and medicine. In recent years several modeling techniques have been developed for reconstruction of digitized representations of the rock microstructures [5,9,13–19]. Using these models effective physical properties such as elastic moduli, electrical resistivity, fluid permeabilities, and constitutive relationships for multiphase flow are computed numerically. For the accuracy of these predictions, it is crucial that the 3D representation of the underlying pore scale microstructure is as realistic as possible.

* Corresponding author at: S.V. College, University of Delhi, Dhaula Kuan, New Delhi - 110 021, India. Tel.: +91 11 2411 2196; fax: +91 11 2411 8535.
E-mail address: biswal@icp.uni-stuttgart.de (B. Biswal).

0378-4371/$ – see front matter © 2010 Elsevier B.V. All rights reserved.
doi:10.1016/j.physa.2009.12.006

Several experimental methods for generating 3D pore scale models exist currently, e.g., combining a series of 2D sections (with spacing no less than 10 μm between the planes) [20], using focused ion beam [21] and through non-destructive μ-CT procedures [22–24]. Several advancements in the computational reconstruction of 3D pore space models have also been proposed. The conditional simulated annealing (CSA) technique has been used to reconstruct a μ-CT of Berea sandstone [25]. A Poissonian penetrable polydisperse sphere model conditioned by the experimental solid size distribution has been developed to analyze the percolation of a low porosity Fontainebleau sandstone [18]. Using the two-point statistics, an exhaustive branching technique is introduced [26]. Using 2D thin sections as training images, a two-point statistics method is enhanced to multiple point statistics [27]. A method of microstructure reconstruction through pattern recognition using support vector machine (a statistical learning algorithm for pattern classification and regression) utilizing the 2D micro-images as training objects has also been developed [28]. A modified Gaussian random field method using convex quadratic programming has been developed to find the optimal admissible autocorrelation function [29].

In this paper we utilize a continuum geometrical modeling technique [10] to reconstruct the pore scale microstructure of a laboratory scale Fontainebleau sandstone. The underlying geological process governing the formation of the sandstone, i.e., the deposition of grains followed by compaction and cementation due to various diagenetic processes are reflected in the algorithm. The model of the sandstone is represented by a list of randomly deposited overlapping quartz crystallites defined geometrically and placed in the continuum. The properties of these crystallites and their nature of packing are defined in the model based on the information gathered from 2D images of the modeled rock.

The paper is organized as follows. The modeling method is described in Section 2 and the procedure to obtain synthetic μ-CT images from the model is described in Section 3. The model implementation along with the model parameters are discussed in Section 4. A comprehensive microstructure characterization of the model and its comparison with similar measurements from experimental μ-CT image of the rock and three other standard reconstruction models are presented in Section 5.

2. The model

We use a continuum geometrical model [10,11,30] originally conceived and used for reconstructing carbonate rock microstructure. Construction and use of a primordial filter function was a critical component of these earlier implementations. The model has never been used for reconstructing sandstones and a primordial filter function is not needed for such microstructure. For completeness, we redefine the model for the sandstones and present this below.

2.1. Continuum representation

In this stochastic geometrical model [10,11,30] the sandstone is represented by a random sequence of points decorated with different types of quartz crystallites. These quartz crystallites are polyhedrons defined geometrically. An element $\omega_i = (\mathbf{x}_i, R_i, \mathbf{a}_i, T_i)$ of the sequence represents a quartz crystallite of type T_i at spatial position $\mathbf{x}_i \in \mathbb{S}$ with an inscribed sphere of radius R_i and orientation $\mathbf{a}_i$. The sample contains g different types of quartz crystallites and a total of N quartz crystallites.

As in Refs. [10,11], the state space of the sandstone containing N crystallites occupying a bounded region $\mathbb{S} \subset \mathbb{R}^3$ is the set

$$\Omega_N = (\mathbb{S} \times [R_{\min}, R_{\max}] \times \mathbb{E} \times \{1, 2, \ldots, g\})^N \tag{1}$$

of all sequences $\omega = (\omega_0, \omega_1, \ldots, \omega_N) \in \Omega_N$ with $[R_{\min}, R_{\max}] \subset \mathbb{R}^1$ and $\mathbb{E} = \{\mathbf{x} \in \mathbb{R}^3 : |\mathbf{x}| = 1\}$. A probability distribution Pr on the space Ω of sequences further specifies the model [10].

2.2. Sedimentation

The points $\mathbf{x}_i$ are chosen randomly in $\mathbb{S} \subset \mathbb{R}^3$ and added sequentially if the following overlap condition is satisfied. For each new point $\mathbf{x}_i$, a sphere of radius $R_i \in [R_{\min}, R_{\max}]$ is chosen randomly and we set $\Pr(\Omega_c) = 0$ for

$$\Omega_c = \{\omega \in \Omega : \exists\, i, j, O(\omega_i, \omega_j) \notin (0, \lambda]\} \tag{2}$$

where the degree of overlap with the sphere at $\mathbf{x}_j$ is measured by

$$O(\omega_i, \omega_j) = \frac{R_i + R_j - |\mathbf{x}_i - \mathbf{x}_j|}{R_i + R_j - |R_i - R_j|}. \tag{3}$$

The parameter λ defines the maximum allowed overlap between two neighboring crystallites. This parameter of the model is related to the amount of compaction in the underlying diagenesis process. Its value is determined from the 2D images from the sandstone. The deposition criteria ensures that each newly added crystallite has a finite overlap with at least one of the existing crystallites, thereby ensuring a fully connected matrix. The total number of points to be deposited for a given volume is specified by a number density ρ, another model parameter that is also determined from the 2D image. The nature of the pore scale microstructure and the total porosity of the modeled volume depend on the degree of overlap, the density of points and the crystallite size distribution.

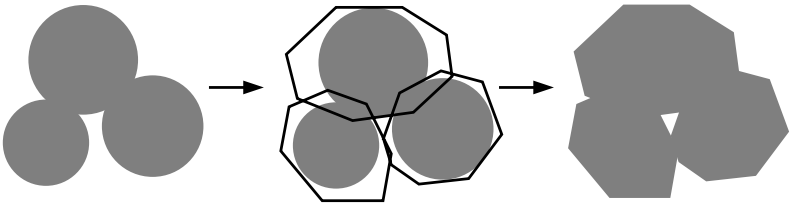

Fig. 1. Schematic representation of the modeling procedure and how it incorporates indirectly the underlying diagenetic process in the sandstone. The deposition of overlapping spheres (sedimentation and compaction) followed by decoration with quartz crystallites (compaction and cementation).

2.3. Diagenesis and compaction

The deposited points are then decorated with quartz crystallites, each of them is a polyhedron defined geometrically by eighteen intersecting planes. More specifically, a quartz crystallite of type T_i with orientation $\mathbf{a}_i$ and size d_i is placed at each point $\mathbf{x}_i$. The sandstone is fully represented by a list of N quadruples $(\mathbf{x}_i, d_i, \mathbf{a}_i, T_i)$. For convergence of the deposition algorithm, the overlap condition in Eq. (2) is defined for spherical volumes associated with each deposited point. This spherical volume is inscribed within the decorated quartz crystallite at that point to retain matrix connectivity. Further, in this model, the shape and the size of the decorated crystallites relate to the amount of compaction and cementation in the underlying diagenetic process. This is determined from image analysis of the available 2D images. The modeling procedure, i.e., the deposition of associated spheres and their replacement by geometrically defined quartz crystallites are schematically shown in Fig. 1.

3. Synthetic micro-CT

The sandstone model is represented by a continuum list of quartz crystallites defined geometrically. Therefore, the model can be discretized at any arbitrary resolution [11]. The discretization process is carried out by subdividing the cubic sample (sidelength ℓ) into a grid of cubic voxels, each of sidelength $a\,\mu$m. Inside each voxel a set of n^3 collocation points, i.e., a $n \times n \times n$ cubic sublattice, is placed symmetrically. The voxel is then assigned an integer label:

- $m = n^3$ if all the n^3 collocation points fall inside the quartz crystallites. This voxel represents matrix.
- $m = 0$ if all the n^3 collocation points fall outside the quartz crystallites. This voxel represents pore space.
- $0 < m < n^3$ if m of the n^3 collocation points fall inside the quartz crystallites. This voxel represents a combination of matrix and pore space.

The voxel label m, therefore, represents the density of the matrix volume in it. As a result, the greyscale grid representation can be called a synthetic μ-CT image of the sandstone model at the resolution $a\,\mu$m. Further, this image can be segmented by choosing a suitable threshold m_c. In such a binary representation, voxels with label $0 < m < m_c$ are relabeled to 0 (pore) and voxels with label $m_c \le m \le n^3$ are relabeled to 1 (matrix). The accuracy of the synthetic μ-CT can be increased by increasing n, the number of collocation points in each voxel.

The computational discretization procedure requires us to determine if a given collocation point falls inside any of the deposited quartz crystallites, i.e., if a point $\mathbf{p}$ falls inside $\mathbb{G}_i$, $i = 1, 2, \ldots, N$, where $\mathbb{G}_i$ is the quartz crystallite at position $\mathbf{x}_i$. This is described in the next section.

4. Model implementation

Each quartz crystallite type (unit size, unrotated) is defined by eighteen intersecting planes defined by the perpendicular vectors

$$\mathbf{n}_i = R_z(\beta_i)\, R_y(\alpha_i)\, (\mathbf{e}_1), \quad i = 1, 2, 3, \tag{4}$$

$$\mathbf{n}_i = R_z(\beta_i)\, R_y(\alpha_i)\, (-\mathbf{e}_1), \quad i = 4, 5, 6, \tag{5}$$

$$\mathbf{n}_i = R_z(\beta_i)\, R_x(\alpha_i)\, (c\mathbf{e}_2), \quad i = 7, 8, 9, \tag{6}$$

$$\mathbf{n}_i = R_z(\beta_i)\, R_x(\alpha_i)\, (-c\mathbf{e}_2), \quad i = 10, 11, 12, \tag{7}$$

$$\mathbf{n}_i = R_y(\beta_i)\, R_x(\alpha_i)\, (\mathbf{e}_3), \quad i = 13, 14, 15, \tag{8}$$

$$\mathbf{n}_i = R_y(\beta_i)\, R_x(\alpha_i)\, (-\mathbf{e}_3), \quad i = 16, 17, 18. \tag{9}$$

In other words, each plane is specified by the unit normal $\hat{\mathbf{n}}_i$ and a point $(\mathbf{n}_{i1}, \mathbf{n}_{i2}, \mathbf{n}_{i3})$. The scale factor c is a random number chosen in the interval [1.3, 1.4] that provides the ellipsoidal shape of the quartz crystallites. $\mathbf{e}_1 = (1, 0, 0)$, $\mathbf{e}_2 = (0, 1, 0)$

and $\mathbf{e}_3 = (0, 0, 1)$ are the unit vectors of the coordinate axes. The three rotation matrices are defined as

$$R_x(\theta) = \begin{pmatrix} 1 & 0 & 0 \\ 0 & \cos\theta & -\sin\theta \\ 0 & \sin\theta & \cos\theta \end{pmatrix}$$

$$R_y(\theta) = \begin{pmatrix} \cos\theta & 0 & \sin\theta \\ 0 & 1 & 0 \\ -\sin\theta & 0 & \cos\theta \end{pmatrix}$$

$$R_z(\theta) = \begin{pmatrix} \cos\theta & -\sin\theta & 0 \\ \sin\theta & \cos\theta & 0 \\ 0 & 0 & 1 \end{pmatrix}.$$

The rotation angles α_i and β_i (in degrees) are chosen randomly in the intervals

$$\begin{aligned}
&\alpha_1 \in [-5, 5], \quad \alpha_2 \in [25, 35], \quad \alpha_3 \in [-35, -25]; \quad \beta_i \in [-5, 5], \quad i = 1, 2, 3 \\
&\alpha_4 \in [-5, 5], \quad \alpha_5 \in [25, 35], \quad \alpha_6 \in [-35, -25]; \quad \beta_i \in [-5, 5], \quad i = 4, 5, 6 \\
&\beta_7 \in [-5, 5], \quad \beta_8 \in [25, 35], \quad \beta_9 \in [-35, -25]; \quad \alpha_i \in [-5, 5], \quad i = 7, 8, 9 \\
&\beta_{10} \in [-5, 5], \quad \beta_{11} \in [25, 35], \quad \beta_{12} \in [-35, -25]; \quad \alpha_i \in [-5, 5], \quad i = 10, 11, 12 \\
&\alpha_{13} \in [-5, 5], \quad \alpha_{14} \in [25, 35], \quad \alpha_{15} \in [-35, -25]; \quad \beta_i \in [-5, 5], \quad i = 13, 14, 15 \\
&\alpha_{16} \in [-5, 5], \quad \alpha_{17} \in [25, 35], \quad \alpha_{18} \in [-35, -25]; \quad \beta_i \in [-5, 5], \quad i = 16, 17, 18,
\end{aligned}$$

where the minimum and the maximum values are chosen so as to qualitatively match the shape with the quartz crystallites seen in the experimental image of the rock. At each position $\mathbf{x}_i$ a quartz crystallite is placed. Its type is chosen randomly from g different types. The number g of different crystallite types should be as large as possible. For our simple model here we have chosen $g = 99$ as a compromise between realism and computational effort. The unit crystallite is scaled by a factor d_i and the rotation of the crystallite is implemented through generalized quaternions. For each quartz crystallite $\mathbb{G}_i,\ i = 1, 2, \ldots, N$, with the origin of the coordinate axes coinciding with $\mathbf{x}_i$, the orientation $\mathbf{a}_i$ is defined by a sequence of three rotations of θ_1, θ_2 and θ_3 about the coordinate axes $\mathbf{e}_1, \mathbf{e}_2$ and $\mathbf{e}_3$ respectively, i.e.,

$$\mathbf{a}_i = \mathcal{Q}_{i3}\mathcal{Q}_{i2}\mathcal{Q}_{i1} = \mathbf{q}_i. \tag{10}$$

The unit quaternion $\mathcal{Q}_{ij}$ represents a rotation of θ_j about the unit vector $\mathbf{e}_j$.

The discretization procedure involves determining if a given point falls inside any of the quartz crystallites. A specific point $\mathbf{p}$ falls inside the crystallite $\mathbb{G}_i,\ i = 1, 2, \ldots, N$, if

$$\mathbf{n}_j \cdot \left(\frac{1}{d_i}\mathbf{p}'_r - \mathbf{n}_j \right) < 0, \quad j = 1, \ldots, 18 \tag{11}$$

where $\mathbf{n}_j$ are the normal vectors that specify $\mathbb{G}_i$, $\mathbf{p}'_r = \mathbf{q}_i^{-1}(\mathbf{p} - \mathbf{x}_i)(\mathbf{q}_i^{-1})^*$ and $(\cdot)^*$ is the quaternion conjugation.

As described in Section 2, the model parameters are the minimum and maximum radii of the spherical volume associated with each point ($R_{\min},\ R_{\max}$), the maximum allowed overlap between two adjacent crystallites (λ), the orientation of the crystallites $\mathbf{a}_i$ defined by the three rotation angles θ_1, θ_2 and θ_3 and the point density ρ. We start with a set of initial estimates of these parameters from the image analysis of a 2D image that is a randomly selected plane from an available μ-CT image of the Fontainebleau sandstone at 7.5 μm resolution. This image is shown in Fig. 2. We first generate a cubic sample of sidelength 5 mm to calibrate the model parameters. The reconstructed model is then discretized at 7.5 μm resolution and thresholded by the Otsu method [31]. The model parameters are then calibrated until the porosity, morphology and other microstructure statistics from the thresholded image from the model match with those measured from the experimental μ-CT image at this resolution.

The model parameters tuned by us are $R_{\min}$, $R_{\max}$ and λ. The packing morphology and the final porosity depend on these parameters. For any specific choice of $R_{\min}$ and $R_{\max}$, the number of deposited crystallites can be increased leading to a decrease in porosity if the overlap parameter λ is increased. For a fixed λ, porosity can be decreased by choosing a large $R_{\max}/R_{\min}$. It must be noted that for very large $R_{\max}/R_{\min}$, the algorithm may take prohibitively long time to converge to an optimal packing of the crystallites as the total number of crystallites will be very large.

The final model parameter values are as follows: $R_{\min} = 80$ μm, $R_{\max} = 170$ μm, $\lambda = 0.15825$. The spherical deposits are optimally packed and the resulting point density is $\rho = 425$ spheres/mm^3. No specific distribution in the crystallite size or orientation were observed in the 2D image. So the radius R_i is chosen randomly from the interval $[R_{\min},\ R_{\max}]$. The three rotation angles θ_1, θ_2 and θ_3 (in degrees) are chosen randomly from the interval $[-90, 90]$ degrees. Finally, $\mathrm{d}_i = R_i$, i.e., the associated spherical volume is just inscribed within the quartz crystallite defined in Eq. (9).

The model is then discretized at a resolution of 7.5 μm by the method described in Section 3 by choosing $n = 6$. This produces a synthetic μ-CT image that is close to an 8-bit greyscale image. A plane from the resulting synthetic μ-CT image, thresholded by Otsu methods [31], is shown in Fig. 2 showing the qualitative similarity between the morphology of the continuum model and that of the original sandstone.

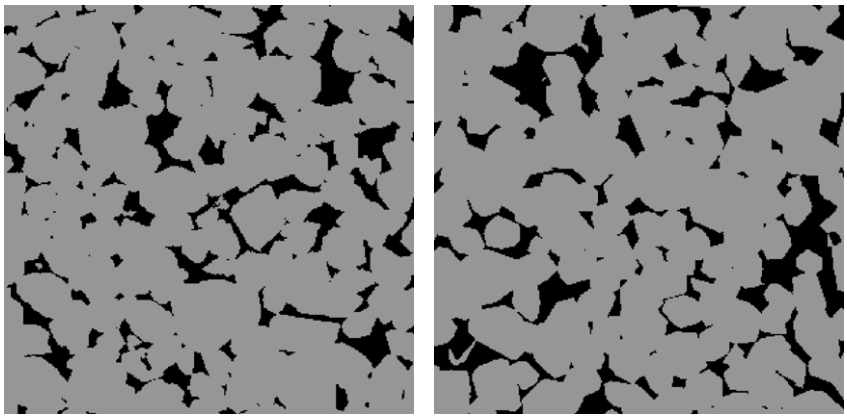

Fig. 2. 2D sections (2.25 mm × 2.25 mm) from the experimental μ-CT image of the Fontainebleau sandstone at 7.5 μm resolution (left) is compared with that from the synthetic μ-CT image of the model at the same resolution (right). Pore space is black and matrix is grey.

Table 1
Minkowski functionals and permeabilities measured on the five samples: Experimental μ-CT (EX, 300 × 300 × 299 voxels), continuum model (CM, 300^3 voxels), diagenesis model (DM, 255^3 voxels), Gaussian filter model (GF, 256^3 voxels) and simulated annealing model (SA, 256^3 voxels).

Sample	Minkowski functionals				Permeability (mD)
	Porosity	Specific surface	Mean curvature	Total curvature	
	$\phi = \phi_3$ (%)	ϕ_2 (mm^{-1})	ϕ_1 (mm^{-2})	ϕ_0 (mm^{-3})	
EX	13.55	9.99000	−151.000	−2159.00	1230
CM	13.54	9.36392	−114.830	−1702.09	1182
DM	13.56	10.3047	−194.245	−2765.57	877
GF	14.21	14.5341	−448.961	4333.62	78.19
SA	13.54	11.0363	−221.549	14484.3	88.19

5. Microstructure characterization and comparison

A 2.25 mm × 2.25 mm section of the sandstone model discretization at a resolution of 7.5 μm is compared with the experimental μ-CT image and also with some of the standard reconstruction models widely used currently. In Ref. [32] the thresholded experimental μ-CT image of the Fontainebleau sandstone (EX) was compared with a process based diagenesis model (DM, Refs. [33,34]), a reconstruction model based on Gaussian Filter technique (GF, Ref. [2]) and a reconstruction model based on Simulated Annealing (SA, Refs. [15,16]). These three models are currently among the standard techniques used to reconstruct the pore scale microstructure of sandstones. All the three modeling techniques could accurately reproduce the porosity (Table 1) and the two-point correlation function (Fig. 4) of the original rock at 7.5 μm resolution. However, as shown in Fig. 3, the morphology of the three models differ significantly from that of the original rock. Quantitative microstructure measurements based on the local porosity theory [35] on the two stochastic models differed significantly from that measured on the μ-CT image of the original rock [32]. In spite of the discrepancy in the morphology, the process oriented modeling approach such as the diagenesis model (DM) was found to be comparatively better than the two stochastic models [32].

The discretization from the continuum model at the resolution of 7.5 μm is thresholded by the Otsu method [31]. Let $\mathbb{S} \subset \mathbb{R}^3$ represent this thresholded discretization image (binary voxels placed on a simple cubic lattice) whose sidelength is M in units of the lattice constant a, the resolution of the discretization process. The two-component porous sample $\mathbb{S} = \mathbb{P} \cup \mathbb{M}$ is the union of two closed subsets $\mathbb{P} \subset \mathbb{R}^3$ and $\mathbb{M} \subset \mathbb{R}^3$ where $\mathbb{P}$ denotes the pore space and $\mathbb{M}$ denotes the matrix space. The characteristic (or indicator) function $\chi_{\mathbb{P}}(\mathbf{x})$ of the set $\mathbb{P}$ is defined as

$$\chi_{\mathbb{P}}(\mathbf{x}) = \begin{cases} 1 & \text{for } \mathbf{x} \in \mathbb{P} \\ 0 & \text{for } \mathbf{x} \notin \mathbb{P} \end{cases} \tag{12}$$

where $\mathbf{x}$ is the position vector of the voxel on the digitized grid.

We present below a comprehensive quantitative microstructure comparison between the original μ-CT image (EX) and the four models (CM, DM, GF and SA). All measurements are carried out on a thresholded 300 × 300 × 300 binary voxel grid representation of a section of the modeled rock at the resolution of 7.5 μm.

5.1. Minkowski functionals

Minkowski functionals are quantitative measures of microstructure used widely in mathematical morphology. For completeness and convenience of the reader, we briefly summarise the general definitions [36] in the Appendix. The four

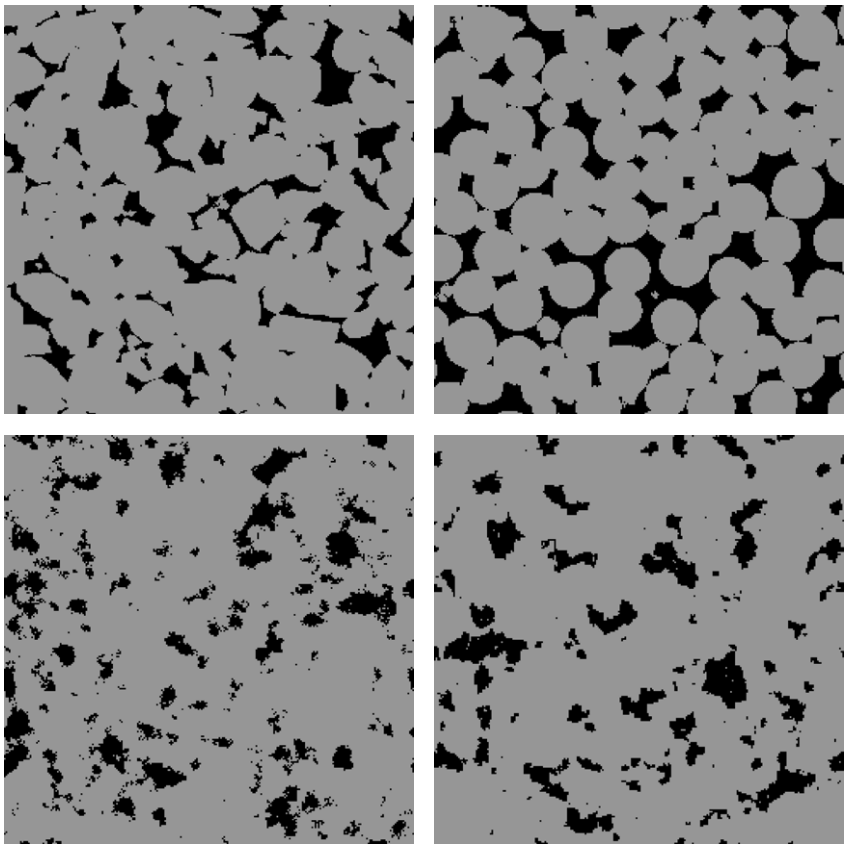

Fig. 3. 2D sections from the experimental μ-CT image of the Fontainebleau sandstone at 7.5 μm resolution (top left) is compared with that from the diagenesis model (DM, top right), Gaussian filter model (GF, bottom left) and simulated annealing model (SA, bottom right) at the same resolution. Pore space is black and matrix is grey.

Minkowski functionals, ϕ_0 (total curvature), ϕ_1 (mean curvature), ϕ_2 (specific surface), and ϕ_3 (porosity) are computed from the four models (CM, DM, GF and SA) and the experimental μ-CT image (EX) using the algorithms developed in Ref. [37]. These are listed in Table 1. The four Minkowski functionals from the continuum model (CM) are in reasonable agreement with that from the μ-CT image. Real quartz crystallites in the Fontainebleau sandstone are of much more complex shape than the simple geometrical definitions of the quartz crystallites adopted in our model. Since the grains in the model are defined by 18 cutting planes, their surface roughness differs from the grains in the original rock. The observed discrepancy is likely because of this. Nevertheless, compared to the other three reconstruction models, the four Minkowski functionals measured from the continuum model are in better agreement with that from the μ-CT image of the rock.

5.2. Two-point correlation function

Assuming homogeneity, the directional two-point correlation functions $C_i(r)$ are defined as

$$C_i(r) = \frac{\langle(\chi_{\mathbb{P}}(\mathbf{x}) - \phi)(\chi_{\mathbb{P}}(\mathbf{x} + r\mathbf{e}_i) - \phi)\rangle}{\langle(\chi_{\mathbb{P}}(\mathbf{x}) - \phi)^2\rangle} \tag{13}$$

where ϕ is the porosity of the sample and $i = 1,\ 2,\ 3$. Their average is $C(r) = \sum_{i=1}^{3} C_i(r)$.

Two-point correlation function along with the porosity are the two most widely used morphological measures for digitized porous media. The slope of the tangent drawn at $C(0)$ provides a rough estimate of the specific surface area of the solid/void and is related to the permeability of the sample [35]. Because of this reason, stochastic models [2,15,16] have focused on matching the porosity and the two-point correlation functions measured from 2D images of the rock with 3D digitized representation of the rock at a specific resolution.

Two-point correlation functions computed from the four models (CM, DM, GF and SA) and the experimental μ-CT image (EX) are plotted in Fig. 4. Over the entire range, the continuum model (CM) and the simulated annealing model (SA) show reasonable agreement with that from the μ-CT image of the rock. It is important to note that SA model is based on the exchange of pore and matrix voxels until a target two-point correlation function is achieved. In the continuum model the match of the porosity (Table 1) and the two-point correlation functions are achieved by adjusting the model parameters.

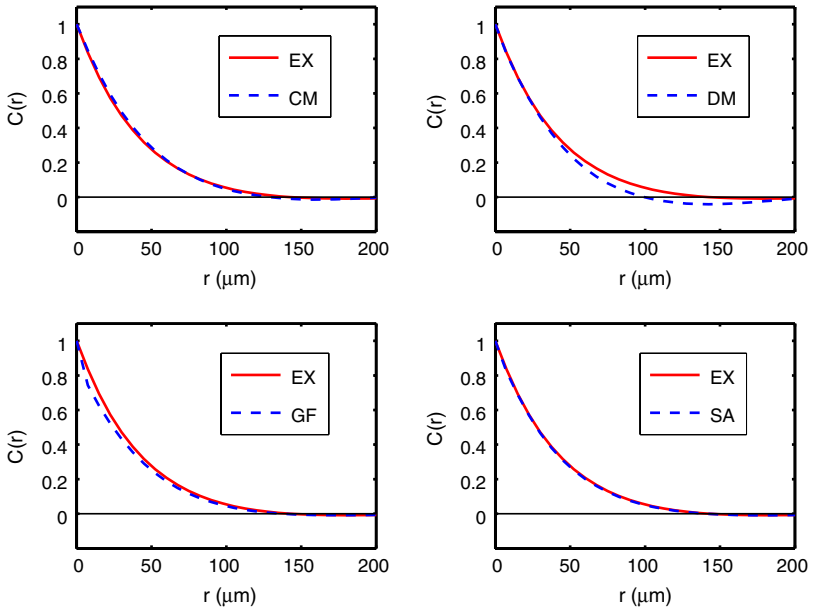

Fig. 4. Averaged directional two-point correlation functions computed from the four reconstruction models compared with that from the μ-CT image of the rock.

At short range, the process oriented diagenesis model also shows reasonable agreement with the original rock. The discrepancy at longer range is due to the anisotropy of the diagenesis model in the z-direction. As shown in Fig. 3, match of the porosity and two-point of correlation function is not sufficient to match the morphology. Among the four models compared here with the original rock, the morphology of the continuum model is closest to the original rock. Although the model appears to be far better for the sandstone microstructure modeled here, the other three models may be more suitable for different classes of microstructure. All these models span a different subset of the vast number of possible microstructures which can arise in nature.

5.3. LPT measurements

A more rigorous scale dependent quantitative microstructure comparison is carried out using Local Porosity Theory (LPT) [1,38]. The usefulness of this method in microstructure characterization of digitized porous media has been established earlier, e.g., comparison of μ-CT images of different sandstones [39] and comparison of 3D models of sandstones with the original [32]. In this method one measures geometric observables such as porosity or connectivity within a compact subset of the porous medium and collect these measurements into various histograms. For the convenience of the reader we briefly repeat the basic definitions of the quantities used in LPT to characterize the porosity and connectivity fluctuations at different length scales in 3D digitized models [35,36].

Within a cubic measurement cell $\mathbb{K}(\mathbf{r}, L)$ of sidelength L centered at the lattice vector $\mathbf{r}$, the local porosity is defined as

$$\phi(\mathbf{r}, L) = \frac{V(\mathbb{P} \cap \mathbb{K}(\mathbf{r}, L))}{V(\mathbb{K}(\mathbf{r}, L))} \tag{14}$$

where $V(\mathbb{K}(\mathbf{r}, L))$ denotes the volume of a subset $\mathbb{K} \subset \mathbb{R}^3$. The *local porosity distribution* $\mu(\phi, L)$ is given by

$$\mu(\phi, L) = \frac{1}{m} \sum_{\mathbf{r}} \delta(\phi - \phi(\mathbf{r}, L)), \tag{15}$$

where m is the number of placements of the measurement cell $\mathbb{K}(\mathbf{r}, L)$ and $\delta(\phi - \phi(\mathbf{r}, L))$ is the Dirac delta function. For adequate statistics $\mathbb{K}(\mathbf{r}, L)$ are placed on all lattice sites $\mathbf{r}$ which are at least a distance $L/2$ from the boundary of $\mathbb{S}$.

A measurement cell $\mathbb{K}(\mathbf{r}, L)$ is termed *percolating in the* x- (y-, z-) *direction* if there exists a connected path lying inside the pore space within the measurement cell between two points on the opposite boundary faces of $\mathbb{K}(\mathbf{r}, L)$ perpendicular to the x- (y-, z-) axis. The connectivity function is defined as

$$\Lambda_c(\mathbf{r}, L) = \begin{cases} 1: & \text{if } \mathbb{K}(\mathbf{r}, L) \text{ percolates in } c \text{ direction} \\ 0: & \text{otherwise.} \end{cases} \tag{16}$$

The function $\Lambda_c(\mathbf{r}, L)$ is measured using the Hoshen–Kopelman algorithm [40]. The *local percolation probability* $\lambda_c(\phi, L)$ is

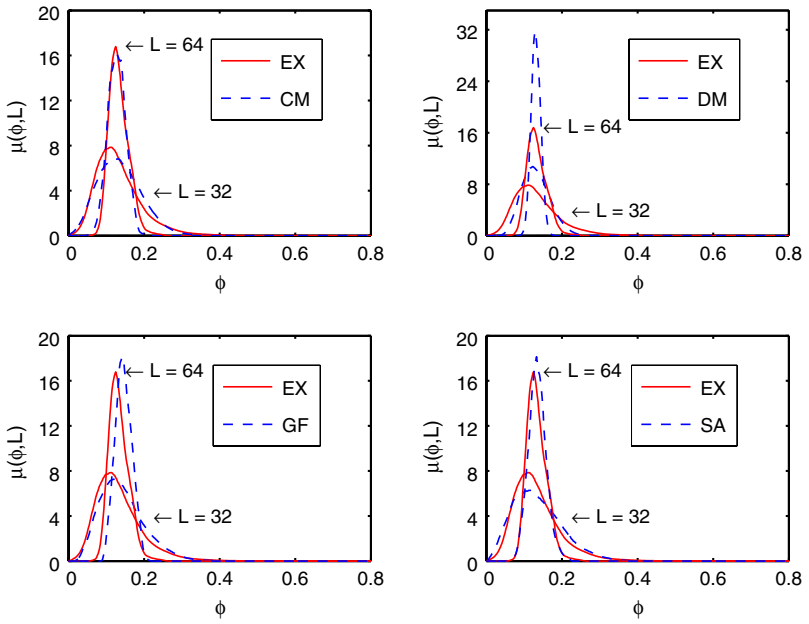

Fig. 5. Local porosity distributions computed from the four reconstructed models compared with that measured from the μ-CT image of the rock. The comparison is presented for two selected sizes of the measurement cells, namely $L = 32$ and $L = 64$ voxel units. Sidelength of the voxel is 7.5 μm.

defined through

$$\lambda_c(\phi, L) = \frac{\sum_{\mathbf{r}} \Lambda_c(\mathbf{r}, L)\delta_{\phi\phi(\mathbf{r},L)}}{\sum_{\mathbf{r}} \delta_{\phi\phi(\mathbf{r},L)}}. \tag{17}$$

It gives the fraction of measurement cells of sidelength L with local porosity ϕ that are percolating in c direction. Here $\delta_{\phi\phi(\mathbf{r},L)}$ is the Kronecker delta. The *total fraction of percolating cells* of size L is given by the integration over all local porosities,

$$p_c(L) = \int_0^1 \mu(\phi, L)\lambda_c(\phi, L)\, \mathrm{d}\phi. \tag{18}$$

The local percolation property is closely correlated with transport properties such as permeability or conductivity as was first pointed out in Ref. [32] and later verified in Ref. [41] for sandstones. It has been systematically used in Ref. [18] for analyzing percolation properties of Fontainebleau sandstone.

Quantities defined in Eqs. (15), (17) and (18) are measured on the four reconstruction models and on the experimental μ-CT image from the original rock. In Fig. 5 the local porosity measurements $\mu(\phi, L)$ are compared for two selected values of L. At each of these measurement cell sizes the local porosity distributions from the continuum model show the closest match with that measured from the μ-CT image of the rock. The process oriented diagenesis model differs significantly from the original rock because of the grain size distribution. The pore sizes correlate strongly with the grain sizes. In the diagenesis model (DM) the grain sizes have small polydispersity compared to the original rock (Fig. 3).

In Fig. 6 the local percolation probabilities $\lambda_3(\phi, L)$ are compared for the same values of L. At each of these measurement cell sizes, the local percolation probabilities (in all three directions) from the continuum model show the closest match with that measured from the μ-CT image of the rock. Equally good agreement is observed for $p_1(L)$ and $p_3(L)$ for all measurement cell sizes as shown in Fig. 7. Both the stochastic reconstruction models (GF and SA) show large discrepancy in comparison to the original rock. These models are based on the two-point correlation function match. Generally the two-point correlation function does not reflect connectivity, in particular not at scales above the correlation length, i.e., between 100 μm to 150 μm (Fig. 4). In Fig. 6 the measurement cell sizes are 240 μm and 480 μm at which the sample has no correlation, therefore is a standard percolation model. Since the porosity is much below the percolation threshold of site percolation, most of the measurement cells are not connected.

The above analysis suggests that at the resolution of 7.5 μm, the pore scale microstructure of the modeled rock matches (quantitatively) very well with that of the experimental μ-CT image. This is further confirmed by the comparison of the absolute permeabilities computed on these five samples (Table 1). The absolute permeabilities are computed by a $D3Q19$ Lattice-Boltzmann single relaxation time method using Darcy's law [42].

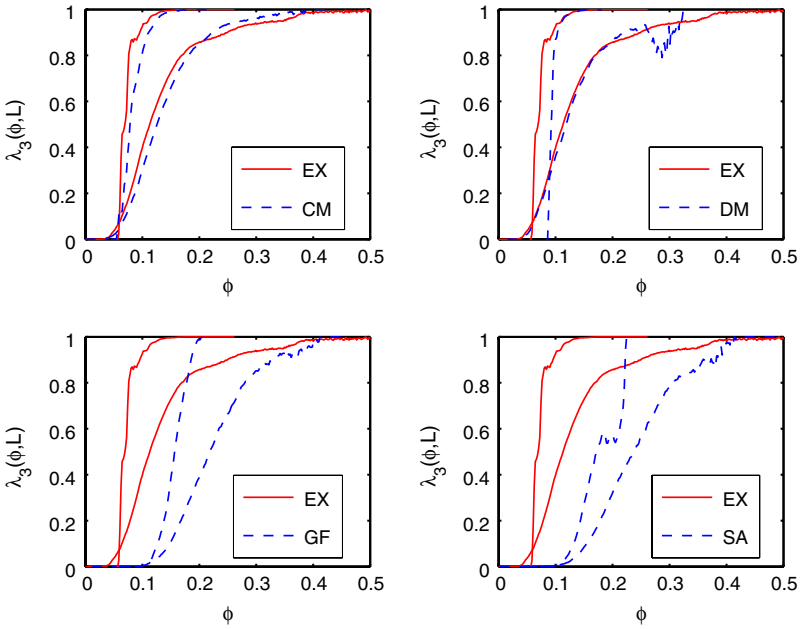

Fig. 6. Local percolation probabilities computed from the four reconstructed models compared with that measured from the μ-CT image of the rock. The comparison is presented for two selected sizes of the measurement cells. For each sample the curve on the right is for $L = 32$ voxel units and the curve on the left is for $L = 64$ voxel units. Sidelength of the voxel is 7.5 μm.

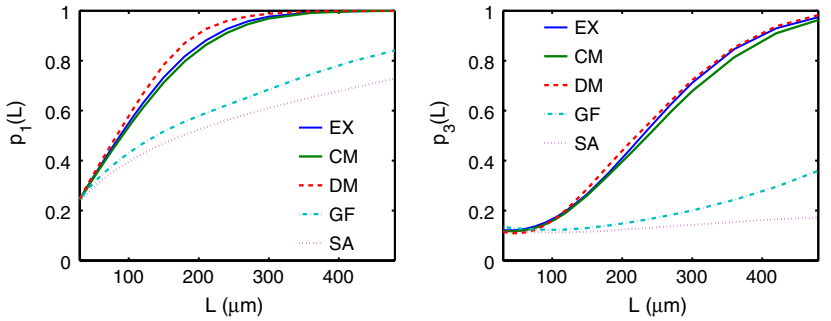

Fig. 7. Total fraction of the percolating cells for the experimental μ-CT image and the four reconstruction models. The quantity $p_1(L)$ plotted on the left corresponds to percolation in any one direction of the measurement cells. The quantity $p_3(L)$ plotted on the right corresponds to percolation in all three directions of the measurement cells.

6. Conclusion

In this work we propose a continuum geometrical modeling approach for reconstruction of 3D pore scale models of sandstones. The method is tested by reconstructing realistic synthetic μ-CT images of the Fontainebleau sandstone at arbitrary resolutions. At a resolution of 7.5 μm, quantitative microstructure measures from the model show impressive match with that measured from the experimental μ-CT image. Both in terms of the morphology and the quantitative microstructure statistics, the continuum model is found to be superior to three other standard reconstruction models. The absolute permeability measured from the model also shows equally good agreement with that measured on the experimental image.

The main shortcomings of the continuum model lie in the geometric definition of the quartz crystallites and their nature of overlap. For modeling simplicity, the quartz crystallites are defined by eighteen cutting planes. For fast convergence, the deposition of the crystallites are carried out by first depositing associated spheres (overlapping) and then replacing them by the quartz crystallites. Compared to the real rock, this procedure leads to somewhat unrealistic packing and orientation of the crystallites in the model. Overcoming this requires process oriented realistic deposition of geometrical objects that closely resemble the quartz crystallites in the original rock. A feasible algorithm for depositing a large number of polydisperse complex shaped overlapping crystallites is not available at this point of time.

Nevertheless, the proposed continuum modeling approach is simple and reproduces the morphology and the quantitative microstructure of the original rock with reasonable accuracy. A major strength of this modeling technique over many standard modeling approaches is the possibility of resolution dependent analysis. The synthetic μ-CT images of the model

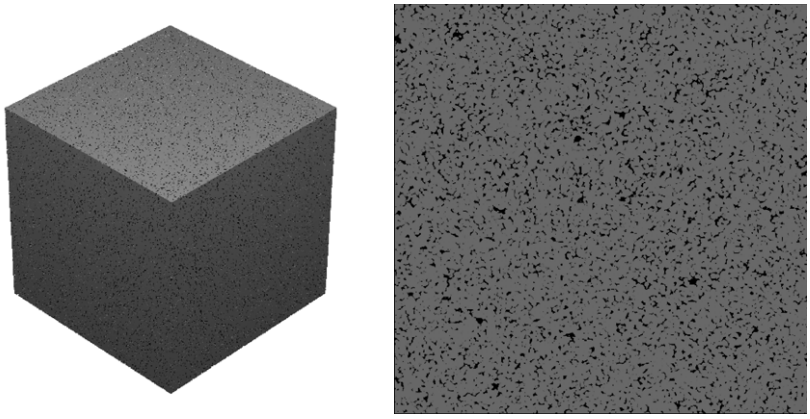

Fig. 8. Left: A laboratory scale cubic sample (sidelength 1.5 cm) generated by the continuum modeling technique. Right: A thin section from the same sample.

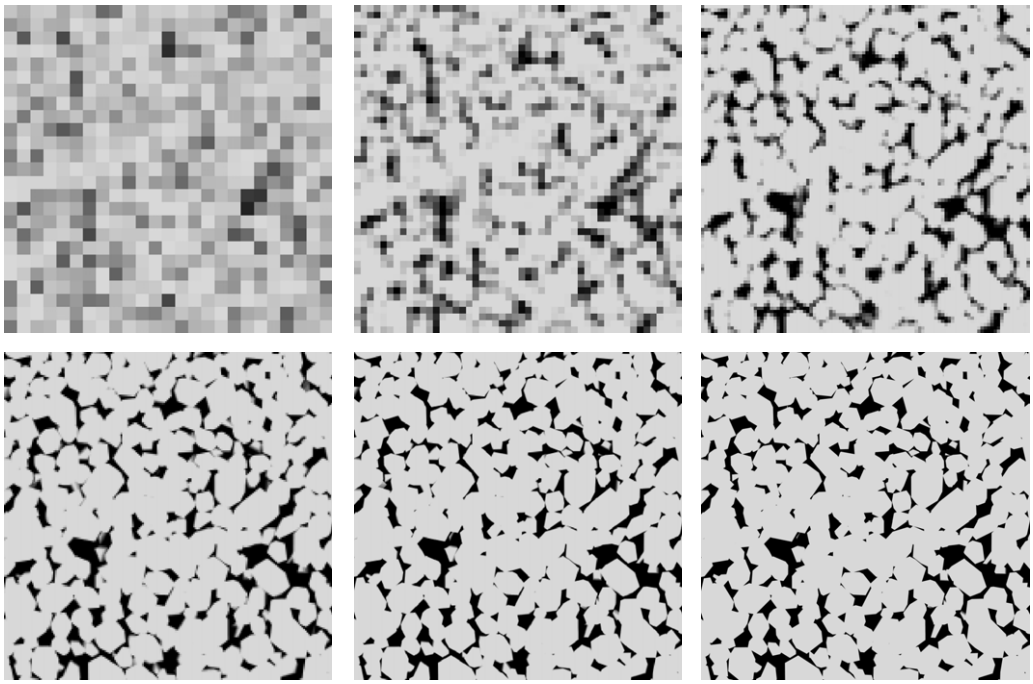

Fig. 9. Synthetic μ-CT images from the model at the resolutions of 120 μm (top left), 60 μm (top middle), 30 μm (top right), 15 μm (bottom left), 7.5 μm (bottom middle) and 3.75 μm (bottom right) showing the gradual resolution of the crystallites. The images are of size 3 mm $\times$ 3 mm.

can be generated at arbitrary resolutions. Because it is not simulated on a grid, pore scale models of large sandstone core plugs can be generated easily. Higher resolution synthetic μ-CT images of the model can be used for more accurate prediction of the petrophysical parameters of the rock.

7. Laboratory scale model

A laboratory scale model of the Fontainebleau sandstone is generated using the calibrated model parameters. The modeled cubic sample has a sidelength 1.8 cm and contains approximately 1.02×10^6 quartz crystallites. A cubic section of sidelength 1.5 cm is cropped from the center of this volume to eliminate the boundary effects. This is shown in Fig. 8. Synthetic μ-CT discretizations of this cubic volume of sidelength 1.5 cm at resolutions of 120 μm, 60 μm, 30 μm, 15 μm, 7.5 μm and 3.75 μm are made available to the scientific community at http://www.icp.uni-stuttgart.de/~hilfer/forschung/. The crystallites are better resolved with increasing resolution as shown in Fig. 9. These noisefree greyscale 3D μ-CT images can be used for studying the dependence of petrophysical properties on the resolution of discretization and also on the method of digitization.

Acknowledgements

FDEL gratefully acknowledges funding from DIKTI, Indonesia. BB and RH are grateful to the Deutsche Forschungsgemeinschaft (SFB 716) and the Stuttgart Research Centre for Simulation Technology (Sim-Tech) for financial support. The authors thank the Scientific Supercomputing Center, Karlsruhe for providing the computing time and technical support.

Appendix. Minkowski functionals

An observable f is a mapping that assigns to each admissible pore space $\mathbb{P}$ a real number $f(\mathbb{P}) = f(\mathbb{P} \cap \mathbb{S})$. If this number can be calculated from $\mathbb{P}$ without solving a physical boundary value problem, then $f(\mathbb{P})$ is a geometrical observable. The set $\mathcal{R}$ of admissible $\mathbb{P}$ is defined as the set of all finite unions of compact convex sets [43,44]. The set of all compact and convex subsets of $\mathbb{R}^d$ is denoted as $\mathcal{K}$. Examples of geometric observables are the volume of $\mathbb{P}$ or the surface area of the internal boundary $\partial\mathbb{P} = \partial\mathbb{M} = \mathbb{P} \cap \mathbb{M}$. Let

$$V_d(\mathbb{K}) = \int_{\mathbb{R}^d} \chi_{\mathbb{P}}(\mathbf{r}) \mathrm{d}^d\mathbf{r} \tag{A.1}$$

denote the d-dimensional Lebesgue volume of the compact convex set $\mathbb{K}$. The volume is hence a functional $V_d : \mathcal{K} \to \mathbb{R}$ on $\mathcal{K}$. An example of a compact convex set is the unit ball $\mathbb{B}^d = \{\mathbf{x} \in \mathbb{R}^d : |\mathbf{x}| \leq 1\} = \mathbb{B}^d(\mathbf{0}, 1)$ centered at the origin $\mathbf{0}$ whose volume is

$$\kappa_d = V_d(\mathbb{B}^d) = \frac{\pi^{d/2}}{\Gamma(1 + (d/2))}. \tag{A.2}$$

Other functionals on $\mathcal{K}$ can be constructed from the volume by virtue of the following fact. For every compact convex $\mathbb{K} \in \mathcal{K}$ and every $\varepsilon \geq 0$ there are numbers $V_j(\mathbb{K}), j = 0, \ldots, d$ depending only on $\mathbb{K}$ such that

$$V_d(\mathbb{K} + \varepsilon\mathbb{B}^d) = \sum_{j=0}^{d} V_j(\mathbb{K}) \varepsilon^{d-j} \kappa_{d-j} \tag{A.3}$$

is a polynomial in ε. This result is known as Steiners formula [43,44]. The numbers $V_j(\mathbb{K}), j = 0, \ldots, d$ define functionals on $\mathcal{K}$ similar to the volume $V_d(\mathbb{K})$. The quantities

$$W_i(\mathbb{K}) = \kappa_i V_{d-i}(\mathbb{K}) \left[\binom{d}{i} \right]^{-1} \tag{A.4}$$

are called quermassintegrals [45]. From (A.3) one sees that

$$\lim_{\varepsilon \to 0} \frac{1}{\varepsilon} (V_d(\mathbb{K} + \varepsilon\mathbb{B}^d) - V_d(\mathbb{K})) = \kappa_1 V_{d-1}(\mathbb{K}), \tag{A.5}$$

and from (A.2) that $\kappa_1 = 2$. Hence $V_{d-1}(\mathbb{K})$ may be viewed as half the surface area. The functional $V_1(\mathbb{K})$ is related to the mean width $w(\mathbb{K})$ defined as the mean value of the distance between a pair of parallel support planes of $\mathbb{K}$. The relation is

$$V_1(\mathbb{K}) = \frac{\mathrm{d}\kappa_d}{2\kappa_{d-1}} w(\mathbb{K}) \tag{A.6}$$

which reduces to $V_1(\mathbb{K}) = w(\mathbb{K})/2$ for $d = 3$. Finally the functional $V_0(\mathbb{K})$ is evaluated from (A.3) by dividing with ε^d and taking the limit $\varepsilon \to \infty$. It follows that $V_0(\mathbb{K}) = 1$ for all $\mathbb{K} \in \mathcal{K} \setminus \{\emptyset\}$. One extends V_0 to all of $\mathcal{K}$ by defining $V_0(\emptyset) = 0$. The geometric observable V_0 is called the Euler characteristic.

For a 3D porous sample with $\mathbb{P} \in \mathcal{R}$ the extended functionals V_i lead to the geometric observables known as Minkowski functionals. The first is the porosity of a porous sample $\mathbb{S}$ defined as

$$\phi(\mathbb{P} \cap \mathbb{S}) = \phi_3(\mathbb{P} \cap \mathbb{S}) = \frac{V_3(\mathbb{P} \cap \mathbb{S})}{V_3(\mathbb{S})}, \tag{A.7}$$

and the second is its specific internal surface area which may be defined in view of (A.5) as

$$\phi_2(\mathbb{P} \cap \mathbb{S}) = \frac{2V_2(\mathbb{P} \cap \mathbb{S})}{V_3(\mathbb{S})}. \tag{A.8}$$

The two remaining observables, the mean curvature $\phi_1(\mathbb{P} \cap \mathbb{S}) = V_1(\mathbb{P} \cap \mathbb{S})/V_3(\mathbb{S})$ and the total curvature $\phi_0(\mathbb{P} \cap \mathbb{S}) = V_0(\mathbb{P} \cap \mathbb{S})/V_3(\mathbb{S})$ have received less attention in the porous media literature.

References

[1] R. Hilfer, Geometric and dielectric characterization of porous media, Physical Review B 44 (1) (1991) 60–75.
[2] P.M. Adler, Porous Media—Geometry and Transports, Butterworth-Heinemann, Boston, 1992.
[3] P.M. Adler, C.G. Jacquin, J.A. Quiblier, International Journal of Multiphase Flow 16 (1990) 691.
[4] P.M. Adler, C.G. Jacquin, J.F. Thovert, Water Resources Research 28 (1992) 1571.
[5] Z. Liang, M.A. Ioannidis, I. Chatzis, Permeability and electrical conductivity of porous media from 3D stochastic replicas of the microstructure, Chemical Engineering Science 55 (22) (2000) 5247–5262.

[6] M.J. Blunt, M.D. Jackson, M. Piri, Valvatne, detailed physics, predictive capabilities and macroscopic consequences for pore-network models of multiphase flow, Advances in Water Resources 25 (2002) 1069.
[7] G. Jin, T.W. Patzek, D.B. Silin, Physics-based reconstruction of sedimentary rocks, Tech. Rep., SPE 83587, 2003.
[8] C.H. Arns, M.A. Knackstedt, K.R. Mecke, Reconstructing complex materials via effective grain shapes, Physical Review Letters 91 (21) (2003) 215506.
[9] J.F. Daian, C.P. Fernandes, P.C. Philippi, J.A.B. da Cunha Neto, 3D reconstitution of porous media from image processing data using a multiscale percolation system, Journal of Petroleum Science and Engineering 42 (1) (2004) 15–28.
[10] B. Biswal, P.E. Øren, S. Bakke, R.J. Held, R. Hilfer, Stochastic multiscale model for carbonate rocks, Physical Review E 75 (6) (2007) 061303.
[11] B. Biswal, P.E. Øren, R.J. Held, S. Bakke, R. Hilfer, Modeling of multiscale porous media, Image Analysis & Stereology 28 (2009) 23–34.
[12] A. Sakellariou, T.J. Sawkins, T.J. Senden, C.H. Arns, A. Limaye, A.P. Sheppard, R.M. Sok, M.A. Knackstedt, W.V. Pinczewski, L.I. Berge, P-E Øren, Micro-ct facility for imaging reservoir rocks at pore scales, SEG Technical Program Expanded Abstracts 22 (1) (2003) 1664–1667.
[13] C.P. Fernandes, F.S. Magnani, P.C. Philippi, J.F. Daian, Multiscale geometrical reconstruction of porous structures, Physical Review E 54 (2) (1996) 1734–1741.
[14] A.P. Roberts, Statistical reconstruction of three-dimensional porous media from two-dimensional images, Physical Review E 56 (3) (1997) 3203–3212.
[15] C.L.Y. Yeong, S. Torquato, Reconstructing random media, Physical Review E 57 (1) (1998) 495–506.
[16] C.L.Y. Yeong, S. Torquato, Reconstructing random media. II. Three-dimensional media from two-dimensional cuts, Physical Review E 58 (1) (1998) 224–233.
[17] C. Manwart, S. Torquato, R. Hilfer, Stochastic reconstruction of sandstones, Physical Review E 62 (1) (2000) 893–899.
[18] J.-F. Thovert, F. Yousefian, P. Spanne, C.G. Jacquin, P.M. Adler, Grain reconstruction of porous media: Application to a low-porosity fontainebleau sandstone, Physical Review E 63 (6) (2001) 061307.
[19] P.E. Øren, S. Bakke, Process based reconstruction of sandstones and prediction of transport properties, Transport in Porous Media 46 (2002) 311–343.
[20] F. Dullien, Porous Media: Fluid Transport and Pore Structure, 2nd ed., Academic Press, San Diego, 1992.
[21] L. Tomutsa, V. Saharon, Focussed ion beam assisted three-dimensional rock imaging at submicron-scale, in: International Symposium of the Society of Core Analysts, 2003, p. 47.
[22] J. Dunsmuir, S. Ferguson, K.D. Amico, Design and operation of an imaging X-ray detector for microtomography, Physics Letters A 121 (1991) 257–261.
[23] P. Spanne, J. Thovert, J. Jacquin, W. Lindquist, K. Jones, P.M. Adler, Synchotron computed microtomography of porous media: Topology and transports, Physical Review Letters 73 (1994) 2001–2004.
[24] M.E. Coles, R.D. Hazlett, E.L. Muegge, K.W. Jones, B. Andrews, B. Dowd, P. Siddons, A. Peskin, P. Spanne, W.E. Soll, Developments in synchrotron X-ray microtomography with applications to flow in porous media, SPE Reservoir Evaluation and Engineering 1 (4) (1998) 288–296.
[25] R. Hazlett, Statistical characterization and stochastic modeling of pore networks in relation to fluid flow, Mathematical Geology 29 (6) (1997) 801–822.
[26] B. Hansen, B. Adams, M. Lyon, A. Henrie, On the reconstruction of polycrystalline microstructures from two-point correlation statistics, Journal of Computer-Aided Materials Design 10 (2003) 163–173.
[27] H. Okabe, M. Blunt, Prediction of permeability for porous media reconstructed using multiple-point statistics, Physical Review A 70 (2004) 066135.
[28] V. Sundararaghavan, N. Zabaras, Classification and reconstruction of three-dimensional microstructures using support vector machines, Computational Materials Science 32 (2005) 223–239.
[29] J. Quintanilla, J. Chen, R. Reidy, A. Allen, Versatility and robustness of gaussian random fields for modelling random media, Modelling and Simulation in Materials Science and Engineering 15 (2007) S337–S351.
[30] B. Biswal, R.J. Held, V. Khanna, J. Wang, R. Hilfer, Physical Review E 80 (2009) 041301.
[31] P.K. Sahoo, S. Soltani, K.C. Wong, A survey of thresholding techniques, Computer Vision, Graphics, and Image Processing 41 (1988) 233–260.
[32] B. Biswal, C. Manwart, R. Hilfer, S. Bakke, P.E. Øren, Quantitative analysis of experimental and synthetic microstructures for sedimentary rock, Physica A 273 (1999) 452–475.
[33] S. Bakke, P. Øren, 3-D pore-scale modelling of heterogeneous sandstone reservoir rocks and quantitative analysis of the architecture, geometry and spatial continuity of the pore network, in: SPE Proceedings, SPE 35479, SPE 35479, European 3-D Reservoir Modelling Conference, Stavanger, Norway, 1996, pp. 11–35.
[34] S. Bakke, P.E. Øren, 3-D pore-scale modeling of sandstones and flow simulations in pore networks, SPE Journal 2 (1997) 136.
[35] R. Hilfer, Transport and relaxation phenomena in porous media, Advances in Chemical Physics 92 (1996) 299–424.
[36] R. Hilfer, Review on scale dependent characterization of the microstructure of porous media, Transport in Porous Media 46 (2002) 373–390.
[37] C. Lang, J. Ohser, R. Hilfer, On the analysis of spatial binary images, Journal of Microscopy 203 (2001) 303.
[38] R. Hilfer, Local-porosity theory for flow in porous media, Physical Review B 45 (13) (1992) 7115–7121.
[39] B. Biswal, C. Manwart, R. Hilfer, Threedimensional local porosity analysis of porous media, Physica A 255 (1998) 221.
[40] D. Stauffer, A. Aharony, Introduction to Percolation Theory, Taylor and Francis, London, 1992.
[41] C. Manwart, U. Aaltosalmi, A. Koponen, R. Hilfer, J. Timonen, Lattice–Boltzmann and finite-difference simulations for the permeability for three-dimensional porous media, Physical Review E 66 (1) (2002) 016702.
[42] J. Harting, T. Zauner, R. Weeber, R. Hilfer, Flow in porous media and driven colloidal suspensions, in: W.E. Nagel, D.B. Kröner, M. Resch (Eds.), High Performance Computing in Science and Engineering '08, Transactions of the High Performance Computing Center, Stuttgart (HLRS) 2008, Springer Verlag, 2008, pp. 349–364.
[43] H. Hadwiger, Altes und Neues über konvexe Körper, Birkhäuser, Basel, 1955.
[44] D. Stoyan, W.S. Kendall, J. Mecke, Stochastic Geometry and its Applications, Wiley-VCH, 1995.
[45] R. Schneider, Convex Bodies: The Brunn–Minkowski Theory, Cambridge University Press, Cambridge, 1993.